PNAS NEXUS

PNAS Nexus, 2025, **4**, pgaf263

https://doi.org/10.1093/pnasnexus/pgaf263
Advance access publication 12 August 2025
Research Report

Mechanical cues guide the formation and patterning of 3D spheroids in fibrous environments

Sharan Sharma[a,1], Atharva Agashe[a,1], Jennifer C. Hill[b], Keya Ganguly[a], Puja Sharma[c], Tara D. Richards[b], Weijian Huang[b,d], David J. Kaczorowski[b,e], Pablo G. Sanchez[f], Rakesh Kapania[g], Julie A. Phillippi[b,h,*] and Amrinder S. Nain[a,c,*]

[a]Department of Mechanical Engineering, Virginia Tech, Blacksburg, VA 24061, USA
[b]Department of Cardiothoracic Surgery, University of Pittsburgh School of Medicine, University of Pittsburgh, Pittsburgh, PA 15219, USA
[c]Department of Biomedical Engineering and Mechanics, Virginia Tech, Blacksburg, VA 24061, USA
[d]Department of Cardiac Surgery, Xiangya Hospital, Central South University, Changsha 410013, China
[e]Heart and Vascular Institute, University of Pittsburgh Medical Center, Pittsburgh, PA 15219, USA
[f]Department of Surgery, University of Chicago, Chicago, IL 60637, USA
[g]Department of Aerospace and Ocean Engineering, Virginia Tech, Blacksburg, VA 24061, USA
[h]Department of Bioengineering, Swanson School of Engineering, University of Pittsburgh, Pittsburgh, PA 15219, USA
*To whom correspondence should be addressed: Email: phillippija@upmc.edu (J.A.P.); Email: nain@vt.edu (A.S.N.)
[1]S.S. and A.A. contributed equally to this work.
Edited By Cristina Amon

Abstract

Multicellular spheroids have shown great promise in 3D biology. Many techniques exist to form spheroids, but how cells take mechanical advantage of native fibrous extracellular matrix (ECM) to form spheroids remains unknown. Here, we identify the role of fiber diameter, architecture, and cell contractility on spheroids' spontaneous formation and growth in ECM-mimicking fiber networks. We show that matrix deformability revealed through force measurements on aligned fiber networks promotes spheroid formation independent of fiber diameter. At the same time, larger-diameter crosshatched networks of low deformability abrogate spheroid formation. Thus, designing fiber networks of varying diameters and architectures allows spatial patterning of spheroids and monolayers simultaneously. Forces quantified during spheroid formation revealed the contractile role of Rho-associated protein kinase in spheroid formation and maintenance. Interestingly, we observed spheroid–spheroid and multiple spheroid mergers initiated by cell exchanges to form cellular bridges connecting the two spheroids. Unexpectedly, we found large pericyte spheroids contract rhythmically. Transcriptomic analysis revealed striking changes in cell–cell, cell–matrix, and mechanosensing gene expression profiles concordant with spheroid assembly on fiber networks. Overall, we ascertained that contractility and network deformability work together to spontaneously form and pattern 3D spheroids, potentially connecting in vivo matrix biology with developmental, disease, and regenerative biology.

Keywords: pericytes, spheroids, cell forces, ECM nanofibers, morphogenesis

Significance Statement

Despite the knowledge that cells produce and respond to their extracellular matrix with organization into 3D tissues, how matrix fiber size, shape, and architecture regulate tissue morphogenesis and function remains incompletely understood. Employing matrix-mimicking fibrous scaffolds, we discover the role of fiber size and spacing in spheroid assembly, patterning, and morphogenesis into complex 3D structures that proceed with dramatic force exertion with requisite matrix deformation. Remarkably, fiber network-induced 3D spheroid assembly activated genes encoding cell–cell, cell–matrix pathways, mechanosensing, and cell contractility, thus exposing the emerging potential of matrix-mediated modulation of cell phenotype and behavior during tissue morphogenesis. These findings are anticipated to broadly impact regenerative medicine, tissue-engineered models of human disease, and drug discovery and testing.

Introduction

3D multicellular aggregates of cells, termed spheroids, have become increasingly popular in vitro platforms for tissue engineering, regenerative medicine, and drug development and screening applications due to their ability to recapitulate in vivo behavior diminished in 2D culture (1–8). Compared with flat 2D cultures, spheroids show differences in mechanical force exertion, biophysical and biochemical signaling, and electrical coupling to influence morphology, motility, proliferation, differentiation, and genetic expression (1, 2 , 4, 9), while being capable of maintaining the phenotype of native tissues for longer durations (3). The past decade has seen tremendous growth in approaches and devices to create spheroids for various applications from disease modeling to cell therapy and regenerative medicine. Despite these advancements in preparing

Competing Interest: The authors declare no competing interests.
Received: May 1, 2025. **Accepted:** July 28, 2025

and maintaining spheroids, how cells leverage mechanical cues (stiffness, curvature, and deformability) from the fibrous extracellular matrix (ECM) to aggregate into spheroids spontaneously remains incompletely understood.

Multiple techniques exist to form spheroids of various cell lineages, including several pluripotent and adult tissue cell lines such as human mesenchymal stem cells, human umbilical vein endothelial cells, murine embryonic stem cells, dermal fibroblasts, chondrocytes, and those from various tumors such as colon, breast, pancreas, and brain (6, 10, 11). Spheroids can be created in scaffold-free cell suspension systems using anti-adhesion substrates or the hanging drop method (3). Various other techniques such as pellet culture, microfluidics, spinner culture, rotating wall vessels, and liquid overlays have also proven effective for assembling spheroids (3, 11). Compared with other methods, spheroids grown within fibrous hydrogels and other polymer matrices that mimic the fibrous environment of native ECM (3, 4, 11, 12) show distinct advantages. For example, human primary hepatocyte spheroids grown in fibrous fibronectin and fibrinogen environments exhibit enhanced cell aggregation and signal transduction (13). The addition of fibers to spheroid cultures enhances their formation and size (14), provides mechanical strength, and increases cell–cell and cell–ECM interactions during aggregation (15, 16). Multiple studies have revealed a distinct role of mechanical cues in spheroid formation (17), growth, and their subsequent interactions with the surrounding fibrous microenvironment (18–23). With endothelial cell spheroids, increasing fiber stiffness promotes sprouting of cells (24). In contrast, porosity dictates whether cells sprout as leader/follower cells (small pore size) or as individual cells (large pore size) (25). By varying fibrinogen and thrombin concentrations, changes in the fiber diameter, fiber crosslinking, and stiffness can influence the invasiveness and sprouting ability of cells from human umbilical vein endothelial cell spheroids (26). Fiber orientation also has a role in influencing aggregate behavior, with oriented fibers showing an increased number of invasive breast cancer cells from tumors (27). Despite these advances, the role of fiber size and network architecture during spheroid formation, growth, and dynamics needs further refinement for a multitude of experimental and translational applications.

This study employed ECM-mimicking suspended fiber nanonets (28, 29) to reveal that fiber size and architecture regulate cell aggregation into spheroids and directly influence their size, shape, and dynamics. We discovered that network deformability, dependent upon the fiber size and architecture, is critical to patterning spheroids at desired locations. Additionally, spheroids assembled around fibers on networks of aligned configurations, and a few cells at the spheroids' edges pulled on the spheroids, causing them to move along the fibers. Using nanonet force microscopy (NFM) (30–32), we report forces during spheroid formation and when individual cells leave spheroids. We developed Boolean outcomes of spheroid merging initiated by the exchange of cells. Our work is motivated by multiple medical challenges, including ischemic diseases, tissue deficits due to congenital defects, disease, injury, and aging, as well as advancements in the design of engineered tissues, which require functional vasculature (33). Our work in tunable assembly of pericyte-derived spheroids builds upon mechanical principles bridging with cell biology (29–31, 34) to direct desired cell behaviors such as exerting proangiogenic activities (35). Furthermore, our approaches are readily amenable to developing personalized medicine approaches for tailored biological therapies that correct ischemic conditions. Overall, we show that fiber network deformability and cell contractility govern matrix mechanical cues that work in tandem to form spheroids through genomic reprogramming, thus connecting matrix biology with developmental, disease, and regenerative biology.

Materials and methods

Fiber network manufacturing and characterization

The suspended fiber networks (aligned and crosshatched) were deposited on hollow metal scaffolds using our previously reported nonelectrospinning Spinneret-based tunable engineered parameters (STEP) technique (36–38). Polystyrene (PS with MW: 2,500,000 g/mol; CAS no. 1025; Scientific Polymer Products, Ontario, NY, USA) was dissolved in xylene (CAS no. 1330-20-7; Carolina, Burlington, NC, USA). Briefly, PS was dissolved in *p*-xylene for at least a week to prepare a polymeric solution for fiber spinning. The solution was extruded through a micropipette (inside diameter ∼100 μm, Jensen Global, Santa Barbara, CA, USA) to deposit suspended and aligned fibers in parallel and crosshatch patterns. We chose the fiber diameters and architectures to match fiber dimensions reported for in vivo matrices. Fibrous ECM in vivo consists of individual fibrils and bundled fibers ranging in diameters from a few hundred nm to several microns (39–41), organized in a diverse range of fiber densities, pore sizes, and network architectures, including aligned configurations (42, 43) and crossing fiber arrangements (44–47). In fibrous environments of large pore sizes, cells make contact with only a few fibers, while in small pore sizes, cells make multiple contacts (48–51). Additionally, the choice of fiber diameters provides a wide range of stiffness values (10–100 nanonewtons/μm) (52). Aligned fiber networks were fabricated by depositing ∼2-μm-thick "base" fibers spaced ∼350μm–1 mm apart, over which orthogonal layers of a parallel array of ∼200/500/800-nm "aligned" fibers with ∼10-μm spacing were deposited (28, 53, 54). Crosshatched fiber networks involved densely spaced (∼10 × 10 μm square pattern) orthogonally deposited layers of fibers having the same diameter (∼200/500/800 nm) (55, 56). The intersections were fused using a custom-solvent system to achieve fixed–fixed boundary conditions at the junctions using tetrahydrofuran. SEM images were taken with a JSM-IT500 InTouchScope scanning electron microscope (JEOL Ltd., Akishima, Tokyo, Japan), and their fiber diameters were characterized.

Cell culture on nanofiber scaffolds

The scaffolds with fiber networks were mounted on 6-well plates (CAS no. P06-1.5H-N; Cellvis, Mountain View, CA, USA), sterilized with 70% ethanol for 10 min, and washed twice with PBS. The suspended fibers and glass bottom were functionalized with 4 μg/mL fibronectin (CAS no. F1141-1MG; MilliporeSigma, Burlington, MA, USA) and incubated at 37 °C for ∼ 1 h to facilitate cell adhesion. We chose to focus primarily on pericytes isolated from the adventitia of the human aorta and associated with the vasa vasorum due to tissue accessibility during cardiac surgery operations. Human pericytes were isolated and culture-expanded as previously described (57) from the adventitial vasa vasorum of the ascending aorta or pulmonary artery resected during heart and/or lung transplantation operations with approval from the institutional review board (University of Pittsburgh protocol #STUDY20040179 and #STUDY21010110) under an informed consent process and deidentified prior to use. Human placental pericytes were commercially obtained (Promocell Inc.). Pericytes were culture-expanded in StemMACS MSC Expansion Media (order no. 130-091-680; Miltenyi

Biotec, North Rhine-Westphalia, Germany) and immortalized using a HPV E6/E7 lentiviral system as previously reported (58). Immortalized pericytes were subcultured from passages 70–85 using 0.1% trypsin–EDTA (CAS no. R001100; ATCC, Manassas, VA, USA) and seeded on fiber networks with a seeding density of ~9×10^4 cells/mL. Additionally, we investigated whether significantly higher cell seeding density affected spheroid formation (Fig. S1). We found that high seeding densities led to monolayer formation by day 21 on all fiber diameters; thus, we chose the lower ~9×10^4 cells/mL as our optimum cell seeding density. Cells were allowed to adhere to the fibers for 30–45 min at 37 °C and 5% CO_2, after which the wells were flooded with 3 mL of culture medium. Media was replenished every second day for up to 21 days. Aortic pericytes were also cultured in the presence or absence of 10 μM or 20 μM Y-27632 (HB2297, Hello Bio Inc, Princeton, NJ, USA), a chemical antagonist of actin–myosin mediated contractility via inhibition of Rho-associated protein kinase (ROCK), dissolved in PBS. Short-term treatment (4 and 8 h) and long-term treatment (1 week) were studied. Y-27632 was then removed, and wells were washed twice with 1 mL of the culture media, followed by the addition of 3 mL of fresh culture media. To examine other cell phenotypes' spheroid formation capabilities, we selected murine fibroblasts and immature human cardiomyocytes. Murine 3T3 fibroblasts (ATCC, catalog no. CRL-1658) were cultured in Dulbecco's modified Eagle medium (DMEM, Corning, catalog no. 10-013-CV) + 10% bovine calf serum (ATCC, catalog no. 30-2030) + 1% penicillin–streptomycin (Gibco, catalog no. 15140-122). Immature human cardiomyocytes (Sigma-Aldrich, catalog no. SCC109) were cultured in DMEM/F-12 MEDIA (1:1, Corning, catalog no. 10-013-CV, Gibco, catalog no. 11765054) +12.5% fetal bovine serum (Corning, 35-015-CF) + 1% penicillin–streptomycin (Gibco, catalog no. 15140-122). Both cell types were cultured at 37 °C and 5% CO_2. Moreover, 0.25% trypsin (Gibco, catalog no. 25200056) was used to lift cells off culture flasks. Both cell types were seeded on fiber scaffolds equivalent to pericytes.

Time-lapse, epifluorescence, and confocal microscopy

Time-lapse videos of seeded scaffolds were obtained using an AxioObserver Z1 microscope (Carl Zeiss, Jena, Germany) with a 20× objective at 5- or 10-min intervals; mosaic images of the entire scaffold were captured with the same objective. Cells and spheroids were fixed with 4% paraformaldehyde, permeabilized in 0.1% Triton X100 solution, and blocked in 5% goat serum. Nuclei were labeled using DAPI (Invitrogen) and F-actin stress fibers using Phalloidin (Alexa Fluor Plus 647 Phalloidin, Invitrogen), while the fibers were labeled prior to seeding via incubation with rhodamine–fibronectin (Cytoskeleton Inc.) for 1 h. Labeled spheroids were imaged in an LSM 880 confocal microscope (Carl Zeiss).

RNA-sequencing library generation and sequencing

Vasa vasorum-associated pericytes were evaluated for gene expression. Monolayer cultured cells and spheroids on fiber networks were lysed after 1, 7, and 21 days of culture. Total RNA was isolated using NucleoSpin RNA kit (Takara/Clontech 740955), followed by cDNA synthesis using high-capacity cDNA reverse transcription kit (ThermoFisher 4368814) and quantification using Qubit ssDNA assay (ThermoFisher Q10212), all performed according to the manufacturer's instructions. It was assessed for quality using an Agilent TapeStation 4150/Fragment Analyzer 5300, and RNA concentration was quantified on a Qubit Flex fluorometer. Libraries were generated with the Illumina Stranded Total Library Prep kit (Illumina: 20040529) according to the manufacturer's instructions. Briefly, 6 ng of input RNA was used for each sample. Following adapter ligation, 15 cycles of indexing PCR were completed, using Illumina RNA UD Indexes. Library quantification and assessment were done using a Qubit FLEX fluorometer and an Agilent TapeStation 4150/Fragment Analyzer 5300. Libraries were normalized and pooled to 2 nM by calculating the concentration based on the fragment size (base pairs) and the concentration (ng/μl) of the libraries. Sequencing was performed on an Illumina NextSeq 2000, using a P3 flow cell. The pooled library was loaded at 750 pM, and sequencing was carried out with read lengths of 2 × 101 bp, with a target of 40 million reads per sample. Sequencing data were demultiplexed by the on-board Illumina DRAGEN FASTQ Generation software.

RNA-sequencing data analysis

Sequences were trimmed according to default settings in the CLC Genomics software with the Molecular Bio plugin (QIAgen), with an additional requirement for a minimum length of 10 nucleotides. Trimmed sequences were aligned to the GRCh38/hg38 human genome reference. Expression browsers were then generated within the CLC Genomics software. Heatmaps were generated using GraphPad software using the Z-score of transcript-per-million (TPM) counts. The raw counts were transformed using the R package "DESeq2'" to calculate the sample-to-sample distance, and a correlation heatmap was generated with the R package "pheatmap."

Quantitative analysis of cell and spheroid behavior on fiber networks

Quantitative analysis of the cells and spheroids from the time-lapse videos and images was performed using ImageJ (NIH; https://imagej.net/). Cell and spheroid boundaries were manually outlined to calculate area and circularity. We used the *circularity* metric to determine the shape of spheroids. Circularity defined as $\left(Circularity = \frac{4\times\pi\times Cell\ Area}{(Cell\ Perimeter)^2}\right)$ ranges from 0 to 1, wherein a value closer to 1 indicates a circular shape, while a value closer to 0 indicates a more "straight-line" shape. We used *persistence* $\left(Persistence = \frac{Displacement}{Total\ distance\ traveled}\right)$ to denote the directionality in the migration of cells and spheroids. A cell or spheroid moving in a straight line without making any turns will have a persistence of one. Cell and spheroid forces were calculated using our established NFM technology (30, 52, 54, 56, 59). This technique involves the use of aligned fiber networks to calculate cellular forces. The thinner *aligned* fibers fused to the stiff *base* fibers on both sides are modeled as fixed–fixed beams. The deflection of the fiber by the cell/spheroid is used to calculate the force exerted on the fibers. Quantification of cell and spheroid migration rates was performed via centroid tracking. Alignment of the nuclear axes within the spheroids was checked against the spheroid axis by manually outlining the nuclear boundary and spheroid boundary from confocal z-stack images. Differences between the major axes of both boundaries were calculated as an angle between 0° and 90°. Student's t tests and ANOVA were used for statistical analysis, with a P-value of <0.05 classified as *, <0.01 as **, and <0.001 as ***. Error bars represent SEs calculated as SD divided by the square root of sample size.

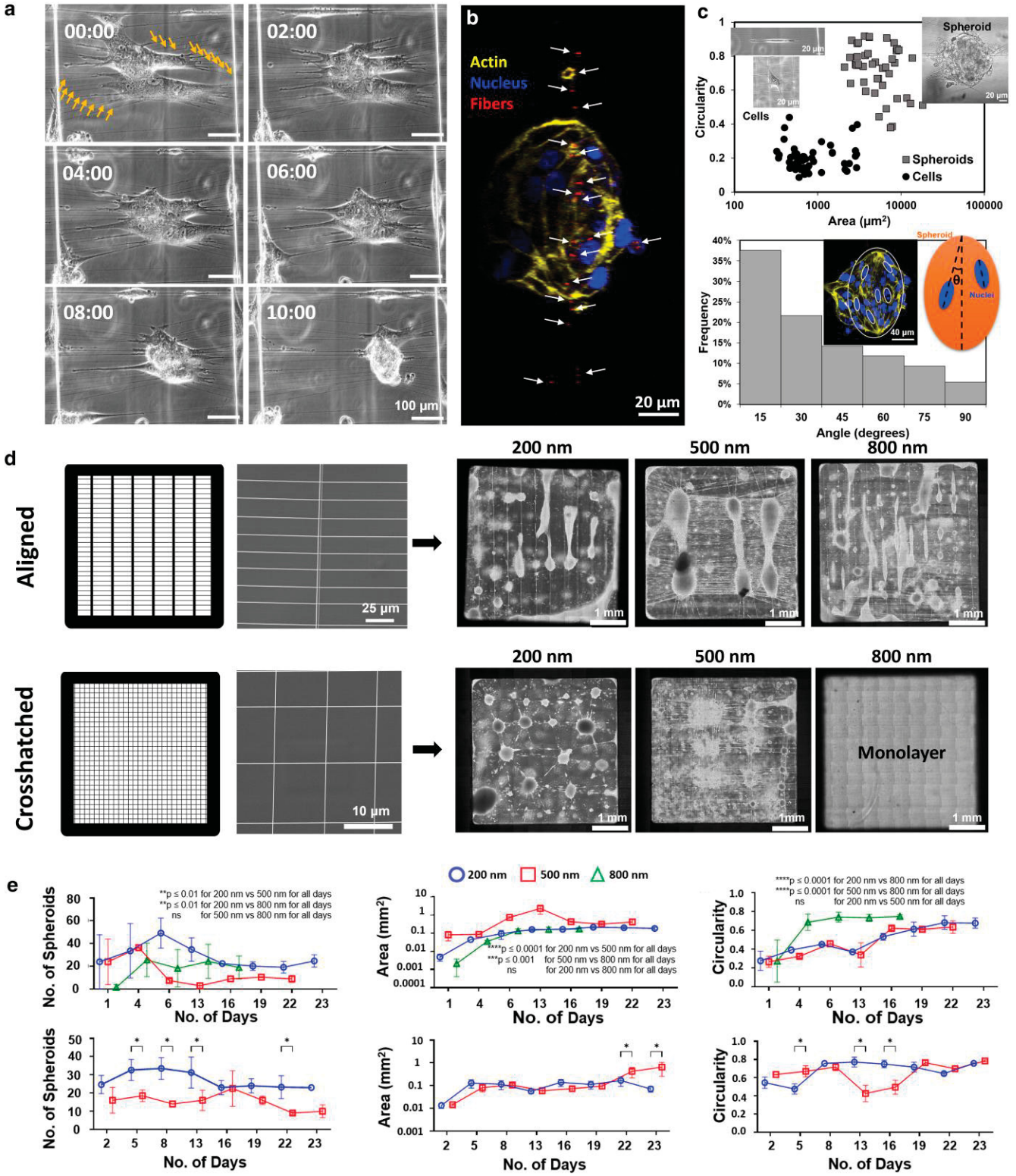

Fig. 1. Pericytes formed spheroids on suspended fiber networks depending on the underlying fiber diameter and architecture. a) Time-lapse images of formation of a spheroid from a group of pericytes on aligned fiber networks (fibers are shown by yellow arrows and time stamps: hh:min). b) Cross-sectional side view of spheroid stained for actin (yellow), nuclei (blue), and fibers (red). The fibers (in red, indicated with white arrows) are present within the spheroids. c) Cells on fiber networks (insets, left) had lower circularities and smaller areas compared with spheroids (inset, right). Sample size of 49 per category. Nuclei within the spheroids have their major axes aligned towards the major axis of the spheroid, indicated by the large number (~60%) of nuclei having a small angle (0°–30°) with the major axes of the spheroid and the nucleus ($n = 388$ [nuclei], $n = 19$ [spheroids]). Insets show a spheroid stained for actin (yellow) and nucleus (blue) and some nuclear boundaries marked in white and a schematic showing the angle between the major axes of the spheroid and the nuclei. d) Pericytes cultured for 2 weeks on aligned and crosshatched fiber networks with 200-, 500-, and 800-nm fiber diameters spontaneously form into spheroids and monolayers depending upon the underlying fiber diameter and architecture. e) Dynamics of spheroid formation shows changes in the number, area, and circularity of spheroids with time when cultured on suspended fibers of varying diameter (200, 500, and 800 nm) and architecture (aligned and crosshatched).

Results

Pericytes aggregate into spheroids on and around suspended fibers

We wanted to inquire whether pericytes aggregated to form spheroids on suspended fibers. We used pericytes as model systems, as members of our team have previously demonstrated that human pericytes derived from ascending aortic vasa vasorum spontaneously self-assemble into spheroids when cultured on Matrigel substrates (57). Pericytes are mural cells predominantly found in the microvasculature with crucial roles in vascular formation and function (60–62), wound healing and regeneration (63), vascular and fibrotic diseases (64), and regulate invasion and vascularization in tumors (65). We cultured aorta-, pulmonary artery-, and placenta-derived pericytes from multiple patients on suspended STEP fiber networks (Fig. S2a–g). We found that pericytes self-assembled into multicellular aggregates (spheroids) (Fig. 1a, Movie S1). Cells applied contractile forces as visualized by the deflection of the fibers during spheroid formation. Compared with single cells or small cell clusters, spheroids were classified as having large areas (~6,187 ± 3,449 vs. 1,066 ± 832 μm^2) and high circularities (~0.71 ± 0.14 vs. 0.21 ± 0.08) ($P < 0.001$, $n = 49$, Figs. 1c and S2h). We used confocal microscopy to visualize spheroid 3D organization on fiber networks coated with rhodamine-conjugated fibronectin. Interestingly, the spheroids were found to aggregate around multiple fibers (above and below the plane of fibers (Figs. 1b and S3a and b). We found that as the area of the spheroids increased, the number of cells within them increased linearly (Fig. S3c, $n = 16$). The nuclear long axes of cells within spheroids were observed to match the long axis of the spheroid, with 38% of the cells having an angle <15° but 60% having an angle <30° ($n = 19$ [spheroids], $n = 388$ [nuclei], Fig. 1c). Lastly, we examined whether nuclei closer to the spheroid center had lower angles when compared with those that were peripheral. We found that for spheroids with an elliptical shape (i.e. low circularity), ~50% of the nuclei had angles ≤30° for distances <30 μm from the spheroids center (Fig. S3d). However, for circular spheroids (i.e. high circularity) ~30–40% of nuclei had angles ≤30° with respect to the spheroid's long axis independent of the distance from the spheroids center, suggesting circumferential alignment of nuclei within the spheroid.

Fiber diameter, architecture, and deformability patterns spheroids

Next, we wanted to inquire whether the size and architecture of fiber networks influenced spheroid formation on fibers. To address this, we tracked pericytes cultured on fiber networks of three diameters (200, 500, and 800 nm; Fig. 1d) in two configurations of aligned and crosshatch networks. We found that, on aligned fiber networks, spheroids formed within 3–7 days of cell seeding regardless of fiber diameter (Figs. S4–S6). To verify this trend, we used aligned 2,000-nm fibers (Fig. S7) and observed the formation of spheroids as well, thus validating that spheroid formation on aligned fibers is independent of the fiber diameter. In multiple instances, we found that cells and cell clusters migrated to the vertical ~2,000-nm *base* fibers and merged to form elongated structures along *base* fibers (Movie S2). During the third week, some of these elongated structures contracted along their major axis into large, individual spheroids at the base fibers (Movie S3). We found that spheroid formation and growth occurred with fiber remodeling, whereby fused junctions were observed to break due to increased contractility, resulting in the merging of parallel fibers (Fig. S8(i)).

Next, we inquired how spheroids formed on a crosshatched network of fibers (two layers of the same diameter fibers orthogonal to each other and fused at the intersections). We found that within crosshatched networks, fiber diameter strongly influenced the cells' ability to aggregate into spheroids (Figs. 1d and S9–S11, ~23 ± 6 [200 nm] vs. 9 ± 1 [500 nm] vs. 0 [800 nm] number of spheroids after 3 weeks of culture, Fig. 1e). Pericyte spheroids formed most readily on 200-nm crosshatched fiber networks (Figs. 1d and S9). Similar to aligned fibers, we observed that the spheroids deformed the fiber networks during growth, with multiple instances of breaking the fused fiber junctions, and remodeling the environment by pulling the fibers closer together (Fig. S8ii, Movie S4). Due to this, we observed that multiple spheroids were joined via interconnecting fibers between them (Fig. S9). Fewer spheroid occurrences were observed after 3 weeks on 500 nm when compared with 200-nm crosshatched fiber networks, resulting in a heterogeneous mix of pericyte spheroids and monolayer regions (Figs. 1d and S10). Regions with more spheroids were associated with broken fiber–intersection junctions and deformed networks, while cell monolayers were observed on intact fibers. Interestingly, pericytes cultured on 800-nm crosshatched networks formed monolayers (minimal to no spheroids), with a high degree of fiber network integrity maintained (Figs. 1d and S11).

Next, from the mosaic images captured every 2–4 days, we calculated various metrics to quantify the dynamics of spheroid cultures (Fig. 1e). On aligned fiber networks, we observed a general trend of an increased number of spheroids by the end of week 1, which was reduced by the end of week 2, presumably due to spheroids merging, which was concomitant with an increase in spheroid area. On 200- and 800-nm aligned fiber networks, we observed multiple long, elongated cellular aggregates on the *base* fibers, which over time became more circular, while on 500-nm aligned fiber networks, we observed elongated structures with extremely large areas that persisted from the second week of culture. In contrast, on crosshatch networks, the 200-nm-diameter fiber category had the highest number of spheroids throughout the 3 weeks of culture. Generally, spheroids formed on a crosshatch network of fibers exhibited high circularity values throughout the 3 weeks in culture, unlike elongated structures predominantly noted at the *base* fibers in aligned configuration during the first and second weeks, which subsequently contracted into spheroids with high circularity. Finally, we inquired whether fiber spacing (dense [≤10 μm] and wide [≥30 μm]) would affect the formation of spheroids on crosshatch networks for the 500 nm and 800 nm diameter fibers. We created custom scaffolds with varying spacing and found that, for both diameters, wider spacing led to the formation of a few spheroids by Day 17, while a monolayer formed in dense regions by Day 10 (Fig. S12).

Observation of the fiber network architecture influencing spheroid formation and our ability to design fiber scaffolds of multiple precise diameters and architectures within one network gave us a unique opportunity to test whether we could achieve control of the spatial patterning of spheroids. We reasoned that a design of monolayer-forming 800-nm crosshatches interspaced with spheroid-forming aligned 200-nm-diameter fiber networks would result in a mix of monolayers and spheroids (Fig. 2a). We observed that spheroids formed only within the aligned fiber regions, and monolayers of cells persisted in regions having crosshatched fiber networks (Fig. S13), thus identifying a new method to create and pattern spheroids using suspended fiber networks. To further explore the influence of fiber networks on the patterning of spheroids, we tested three additional architectures (Figs. 2b(i–iii) and S14–S16). First, we experimented with 200-nm aligned fibers with 10-μm spacing, with a region of crosshatch fibers of the same diameter and spacing near the edges (Fig. 2.b(i)). In line with our earlier observations, we found the aligned region promoted multiple spheroids, and the

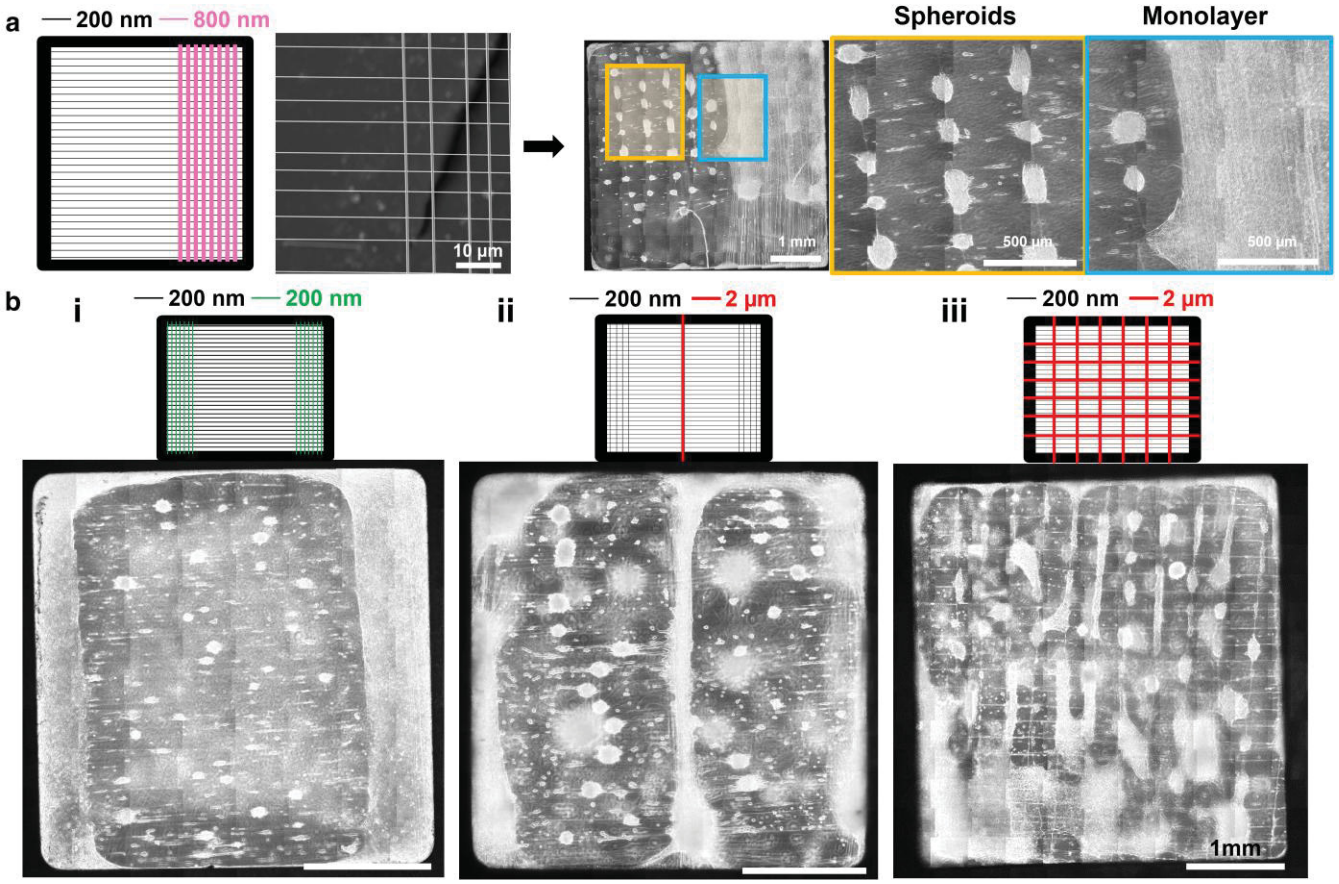

Fig. 2. Patterning of spheroids on fiber networks. a) Pericytes cultured for 2 weeks on fiber scaffolds having both crosshatch and aligned regions on the same scaffold. Regions with aligned fiber architectures show multiple spheroid and aggregate formations, while those with crosshatch fiber networks show monolayer formation. b) Illustration and images of pericyte spheroids formed on (i) ~horizontal 200- and crosshatch ~200-nm-diameter fiber networks of low deformability, (ii) horizontal ~200-nm- and a single vertical ~2-μm-diameter fiber, and (iii) ~horizontal 200-nm- and (horizontal and vertical) 2-μm-diameter fibers (scale bars: 1 mm).

dense crosshatch regions of low deformability promoted cell monolayers. Next, we introduced a single 2-μm fiber near the center of the aligned fibers (red line in the cartoon in Fig. 2.b.(ii), which regionally constrained areas of spheroid formation. While the number of spheroids formed did not vary on either side of the large diameter fiber, their area increased when compared with the scaffolds without the single base fiber (S17). We found the 2-μm fiber to support a dense aggregate of cells. Next, we increased the number of 2-μm fibers along and orthogonal to the 200-nm-diameter aligned fiber networks shown in Fig. 2b(iii). We found that adding larger-diameter fibers slightly increased the number of spheroids. Still, the area of the spheroids was reduced compared with fiber networks of homogenous 200-nm-diameter aligned fibers (Fig. S17). In this configuration, we observed that the 200-nm-diameter fibers were deformed, and the large-diameter fibers defined the boundaries of many spheroids.

We extended our studies to two other cell types: NIH 3T3 and immature human cardiomyocytes. We found 3T3 fibroblasts to form spheroids in aligned fiber configurations and cardiomyocytes on 200-nm aligned and crosshatch scaffolds (Fig. S18). Overall, we demonstrate that through the design of fiber networks, we were able to achieve patterning of spheroids of multiple cell types.

Spheroids exhibit dynamic interactions with their surrounding microenvironment

Next, we inquired how spheroids dynamically interacted with individual pericytes and the microenvironment using time-lapse imaging over short intervals (~8–24 h). On aligned fiber networks, we observed an unusual sliding/migration of spheroids along the fibers (Fig. 3a(i), Movies S5–S7 for pericytes and Movies S8 and S9 for NIH 3T3s). In pericyte experiments, we observed multiple spheroids moving from the horizontal and softer 200-nm aligned regions towards the vertical and stiffer 2-μm *base* fibers (durotaxis). Spheroids were observed to be pulled by a single or a few pericytes (Movies S6 and S7), while in other cases, the pericytes apparently responsible for pulling the spheroids were not visible (Movie S5). Once on the larger diameters, the spheroids grew in size and generally did not migrate back to the smaller diameter fibers (Movies S10 and S11). We tracked the migration speeds and persistence (ability to move in the same direction) of the spheroids. We found them to migrate slower with lower persistence than individual pericytes (Fig. 3a(ii), (iii)).

We also observed individual cells sprouting and using the fibers as highways to migrate away from the spheroids (efflux) or migrate towards (influx) and join neighboring spheroids (Fig. 3b(i), Movies S2, S10, S11 for pericytes, and S12 for cardiomyocytes). We selected spheroids randomly to quantify cellular efflux and influx and found that cell efflux over 24 h was higher ($P = 0.01$) than influx (~25 ± 3 vs. 14 ± 2, $n = 18$) (Fig. 3b(ii)). Over 24 h, we calculated the net outward cell movement, which is the cumulative difference between the cells migrating away and those migrating into the spheroid from other neighboring spheroids. We found that the spheroid area remained consistent with increasing net cell efflux but increased rapidly as efflux decreased (Fig. 3b(iii)). Interestingly, the net cell efflux rate was moderately correlated

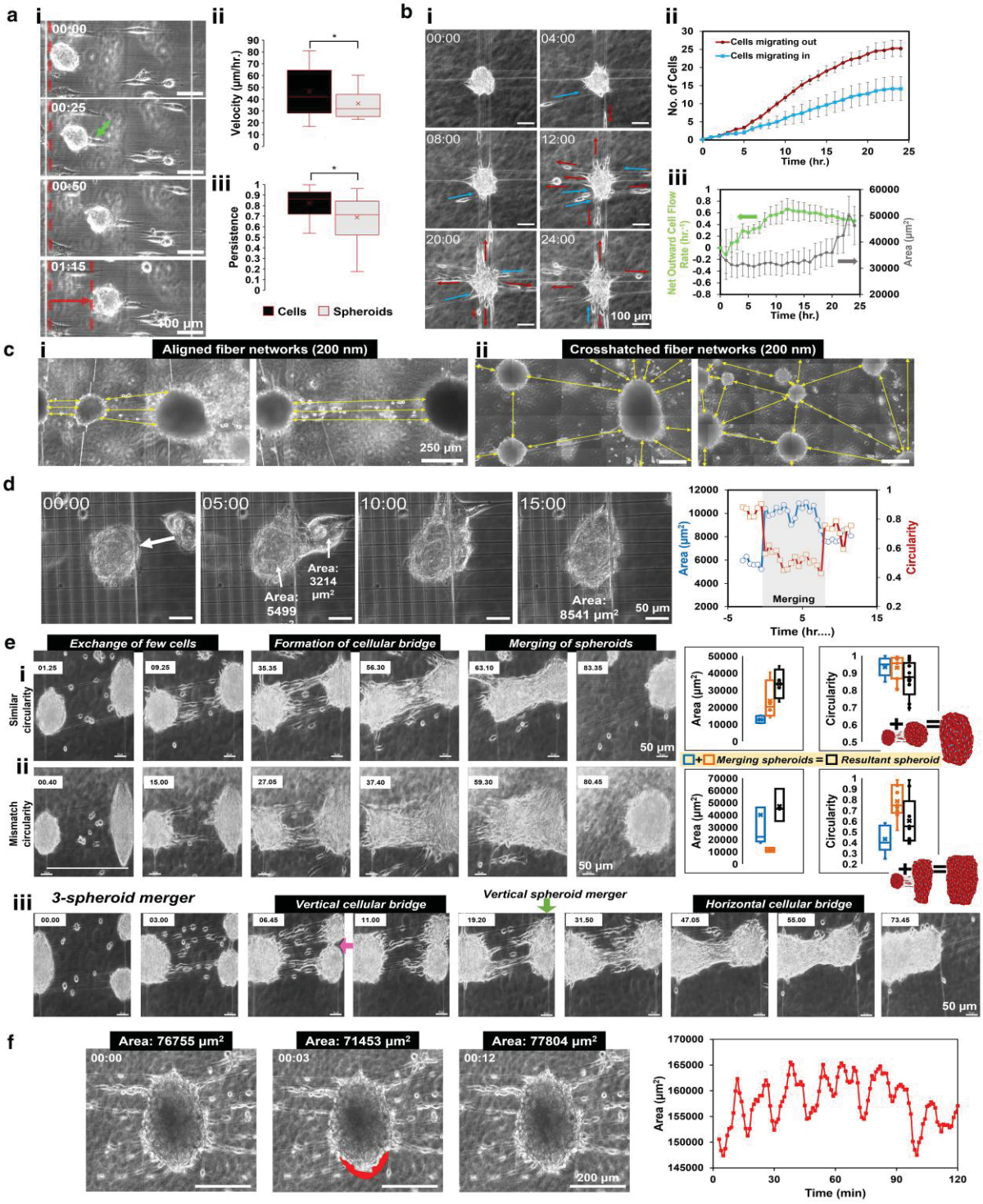

Fig. 3. Spheroid migration, influx/efflux, and spheroid–spheroid interactions on fiber networks. a) (i) Time-lapse images of spheroids migrating along aligned fibers (scale bar: 100 μm); (ii) average velocity (μm/h); and (iii) average persistence of migrating spheroids compared with individual cell migration ($n = 23$). b) (i) Time-lapse images of cells continuously moving into (blue arrows) and moving out of (red arrows) individual spheroids (scale bar: 100 μm); (ii) cells migrating out of spheroids occurred with a higher frequency than cells migrating into the spheroid over time ($n = 18$, error bars represent SE); and (iii) changes in outward cell flow rate and area with time in spheroids when cells are moving into and out of spheroids ($n = 18$, error bars represent SE). c) Extensive remodeling of the fibers during spheroid formation and growth lead to fiber interconnections formed between spheroids (shown with yellow arrows) in both (i) aligned and (ii) crosshatched fiber networks (scale bar: 250 μm). d) Two spheroids merging into each other (scale bar: 50 μm) and the associated changes in area and circularity of the larger (left) spheroid during merging. e) Boolean morphogenesis outcomes and area/circularity analysis of spheroid mergers for cases of two spheroids of (i) similar circularities (circular–circular) and (ii) different circularities (circular–elongated). In both cases, time-lapse images show merger to start with exchange of cells along fibrous highways followed by formation of a "cellular bridge" and eventual merger ($n = 15$ for each category). (iii) Time-lapse images of a three-spheroid merger, with two spheroids on the same base fibers merging first through the formation of a vertical cellular bridge (pink arrow). The resultant vertical spheroid merger (green arrow) then merges with a third spheroid on a different base fiber. f) Asynchronous contractions of a spheroid with data showing beating frequency over a 2-h period. Red shaded area indicates areal loss during contraction (all time stamps in hh:mm).

with the area of the spheroid ($R^2 = 0.62$, Fig. S19). The exchange of cells between spheroids on both aligned and crosshatched fiber networks was found to be facilitated by extensive remodeling of the fiber networks (Fig. 3c(i),(ii)), resulting in numerous spheroid mergers. The greater deformability of the crosshatch networks was associated with larger separation distances between individual spheroids. We did not find any correlation between spheroid separation distance and cellular efflux and influx rates over a 24-h period (Fig. S20).

We developed Boolean outcomes of spheroid mergers (morphogenesis) that occurred either between migrating spheroids of high circularities (Fig. 3d and Movies S13 and S14 for pericytes, Movie S15 for NIH 3T3, and Fig. S21) or between nonmigratory spheroids (Fig. 3e) of similar circular shapes (Movie S16) and between elongated and circular spheroids (Movies S17, S18, and S19). In all mergers, the resultant spheroid increased in area but had a drop in circularity immediately after the merger, which eventually recovered (Fig. S21). In the case of nonmigrating spheroid mergers, we observed that the merger occurred by the active exchange of cells along the fibers connecting them. The merger started with the exchange of a few cells that dramatically increased over time, leading to the formation of a cellular bridge connecting the two spheroids (Fig. 3.e(i), (ii)). Notably, we observed the cell alignment in the cell bridge to be along the fiber axis, which was almost orthogonal to the orientation in the spheroids. After the merger, cells realigned along the spheroid axis. We found that circular–circular spheroid mergers (high circularity, Fig. 3e(i)) surprisingly resulted in only a slight drop in circularity of the merged spheroid. In contrast, low-high circularity (elongated and circular) spheroid mergers resulted in an intermediate range of circularities (Fig. 3e(ii)). We observed spheroid mergers at distances greater than 400 μm and cell bridges forming up to 2 mm long (Fig. S22). We also observed three-spheroid mergers (two spheroids on the same large base fiber connected through aligned fibers to another spheroid on a different base fiber). In such cases, the two spheroids on the same base fiber merged first, followed by the resulting spheroid merging with the spheroid on the separate base fiber. In both mergers, the sequence of exchange of cells followed by the formation of cellular bridges was maintained in both the vertical and horizontal directions (Fig. 3e(iii) and Movies S20 and S21).

In multiple instances, we observed an unusual contraction of the pericyte spheroids causing rhythmically visible deformation of the fiber network (red shaded area showing reduced area after contraction in Fig. 3f and Movies S22 and S23). The pulsing of the spheroids was found to occur in large spheroids (average area: $46{,}208.86 \pm 16{,}282.12\ \mu m^2$). The spheroids contracted and expanded continuously with an average pulse area reduction of $2{,}108.27 \pm 855.46\ \mu m^2$ and a frequency of 4.5 ± 0.74 beats/h. Lastly, we measured whether spheroid beating amplitude and frequency were affected by fiber diameter. We found that beating frequency was lower in 800-nm-diameter fibers when compared with 200- and 500-nm-diameter fibers; however, there was no significant difference in beating amplitude between the three fiber diameters (Fig. S23).

Overall, we demonstrate ECM–deformability directed multiple cell–spheroid, spheroid–spheroid, and spheroid–fiber interactions that led to their migration, mergers, and pulsatile contractions.

Forces and contractility in spheroids

Since pericyte aggregation proceeded with the deformation of fiber networks, we inquired about the contractile nature of spheroids. Using NFM (30, 32, 54, 56), we studied the forces involved during the spheroid assembly by calculating the transient forces from the point when multiple individual cells came into contact with each other until spheroids formed (Movie S1). As the collective area occupied by the cells decreased from the beginning of spheroid formation to when spheroids were fully formed ($14{,}778 \pm 2{,}614$ vs. $8{,}012 \pm 947\ \mu m^2$, $P = 0.02$, $n = 18$), the forces exerted on the fibers decreased ($1{,}294 \pm 466$ vs. 301 ± 368 nN, $P = 0.07$) (Fig. 4a(i)). We also found force exertion to be higher ($P < 0.001$) for spheroids than individual pericytes (Fig. S24a): individual cells had an average force of ~50 nN ($n = 23$), while spheroids exhibited a more comprehensive range of forces (tens of nN–μN). Spheroid forces increased with area (Fig. 4a(ii), $n = 49$). We examined the force distribution within spheroids and found that forces were highest at the peripheral fibers and lowest towards the center (Fig. S24b). We found that cell efflux from larger spheroids led to a decrease in force exertion by ~45% ($P = 0.2$, $n = 21$) and a decrease in area by an average of 14% ($P = 0.006$, $n = 21$, Fig. 4a(iii)).

Next, we interrogated the role of cell contractility in spheroid formation via pharmacological inhibition of ROCK using Y-27632 for 4 h (Figs. 4b and S25). We observed a rapid loss of spheroid compactness (within 1–2 h) and increased cell migration away from the spheroid along the aligned fibers (red arrows in Fig. 4b(ii) and Movie S24), causing an increase in the area and a decrease in the circularity of treated spheroids (Fig. 4c (i), (iii)). The addition of Y-27632 also reduced the force per unit area exerted by spheroids on fibers (2.66 vs. $0.73\ nN/\mu m^2$, $n = 10$, $P = 0.02$) (Fig. 4c(ii)). The effect of ROCK inhibition on spheroids was reversible, as the cells reformed spheroids within 6–8 h after drug wash-out (arrows in Fig. 4b(iii)). Increasing the dose of Y-27632 from 10 to 20 μM and extending the treatment duration from 4 to 8 h maintained the spheroid disassembly (Fig. S26 and Movie S25). ROCK inhibition at the time of cell seeding on fiber networks prevented spheroid formation and caused the pericytes to grow in monolayers (Fig. 4d). After a week of culture in the presence of Y-27632, drug wash-out resulted in cells forming spheroids and elongated structures at multiple locations within 24 h (Movies S26 and S27), similar to control cultures.

Next, we inquired whether gene expression changes accompanied spheroid assembly on suspended fiber networks. RNA sequencing (RNA-Seq) of pericytes collected from force fiber scaffolds and monolayer cultures at days 1, 7, and 21 postseeding revealed differentially expressed genes involving adhesion, mechanosensing, and contractility. The RNA-Seq data revealed increased transcripts of cadherins (Fig. 5a) and integrins (Fig. 5b) at days 1 and 21 of culture on nanofiber scaffolds relative to pericytes maintained in monolayer culture. Additionally, the majority of mechanosensing gene transcript levels (Fig. 5c) were elevated at all three time points in nanofiber culture when compared with monolayer-cultured pericytes. Of note, ROCK1 was upregulated in pericyte spheroids on fiber networks, up through day 21. Notably, all mechanosensing genes were decreased in day 21 monolayer cultured cells compared with other monolayer timepoints and with any nanofiber scaffold timepoint (Fig. 5d). By day 7 and continuing through day 21 in culture, pericytes cultured on nanofiber scaffolds up-regulated transcripts of contractility-related genes when compared with monolayer cultured pericytes.

Overall, we report the ability to measure forces during spheroid formation and point to cell–cell, cell–matrix, mechanosensing, and cell contractility in the maintenance of spheroids on suspended fiber networks.

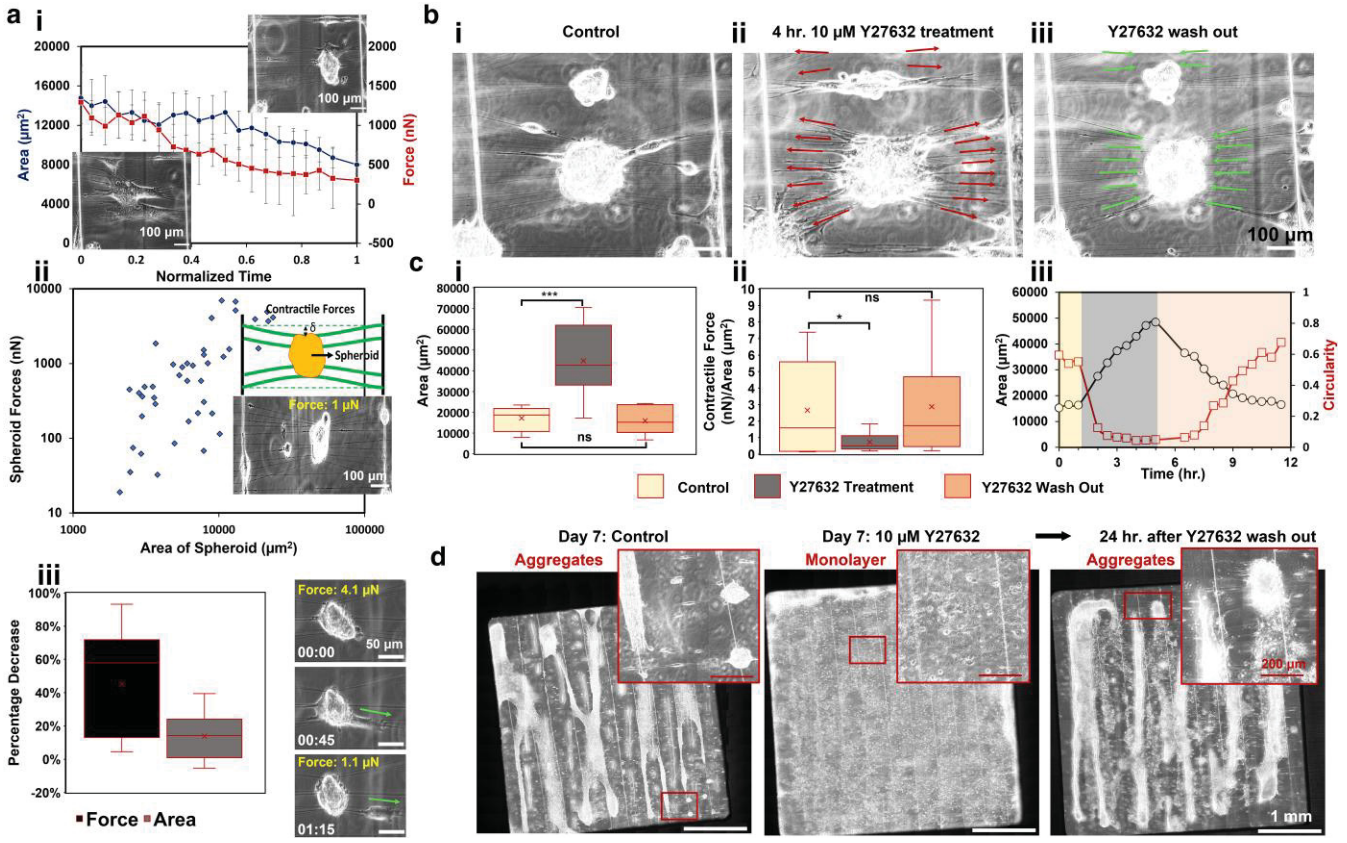

Fig. 4. Contractility of spheroids on fiber networks. a) (i) Clusters of cells (inset, left) undergo dynamic changes in contractile forces and area ($n = 18$) during formation of a spheroid (inset, right) (error bars: SE; inset scale bars: 100 μm). (ii) Spheroid forces with respect to area of the spheroid ($n = 49$). Inset: A representative schematic and image of fibers being deflected by spheroids (top) and a pericyte spheroid (bottom) deflecting the aligned fibers by exerting contractile forces (scale bar: 100 μm). The displacement of the fibers is converted to forces through the stiffness of the fibers modeled as fixed–fixed beams. (iii) Percentage decrease in contractile forces and area of spheroids after an individual cell sprouts out of the spheroid ($n = 21$). Inset images show an individual cell (marked by arrows) sprouting out of a spheroid (scale bar: 50 μm, time stamps: hh:min). b) (i) Spheroids before Y27632 treatment, (ii) effect of treatment of 10 μM Y27632 (ROCK inhibitor) for 4 h on spheroids. Cells within the spheroids lose their contractility and are seen coming out of the spheroid (indicated by arrows), and (iii) recovery of the spheroids after drug wash off. The cells regain contractility and move back into the spheroid (indicated by arrows) by 12 h (scale bars: 100 μm). (c) Changes in (i) area and (ii) contractile forces per unit area during Y27632 treatment and after Y27632 wash out ($n = 10$). (iii) Dynamic changes in area and circularity of the spheroids during Y27632 treatment and after Y27632 wash out ($n = 10$). d) Images of the suspended fiber networks after 7 days of control cultures that have formed aggregates and cells seeded with Y27632 that have formed monolayers. Spheroid/aggregate formation is seen after 24 h of Y27632 wash out similar to control cultures. Insets show a magnified area of the fiber network shown in red box.

Discussion

Here, we demonstrate the dynamic influence of biophysical cues on the formation, growth, and behavior of 3D spheroids of various lineages (pericytes, fibroblasts, and cardiomyocytes) formed spontaneously on ECM-mimicking suspended fiber networks. To evaluate the competing effects of fiber diameter and architecture on spheroid assembly, we designed our scaffolds in two configurations (aligned and crosshatched) of three diameters (200, 500, and 800 nm). Both networks are composed of two-layer structures: in aligned configurations, large 2,000-nm-diameter fibers spaced at least 350 μm apart form a supporting layer on top of which aligned fibers are deposited, while in crosshatch networks, the two layers of the same diameter are deposited to achieve 10×10 μm square patterns. In both configurations, the intersection points of fiber layers are fused; thus, a network of aligned 200 nm and crosshatched 800 nm has the highest and lowest deformability, respectively. We found that matrix remodeling was critical for spheroid formation. Aligned fiber networks promoted formation of spheroids of varying morphologies (circular to elongated) independent of fiber diameter, whereas crosshatched networks showed that increasing the fiber diameter reduced the number of spheroids, with an absence of spheroid formation on 800 nm diameter networks. We think that the increased deformation of small-diameter crosshatch fiber networks leads to local stiffening of the ECM at the intersection points, which causes accumulation of cells as localized monolayers that serve as nucleating sites for spheroid formation. Cells in this configuration do not move away due to durotactic responses. On nondeforming networks, the isotropic distribution of stiffness is responsible for the formation of monolayers. These observations provided us with critical insights across a variety of cell types, allowing us to test and confirm our hypothesis that controlling fiber deformability would lead to the patterning of spheroids at desired locations (summary figure, Fig. 6); accompanied by striking changes in force generation and remarkable shifts in gene expression profiles. We also demonstrate spheroid formation of two different cell types (NIH 3T3) and immature cardiomyocytes (AC 16), which had differences in spheroid formation and dynamics, potentially due to differential mechanosensing of the cell types.

Fibrous matrix properties have been shown to impact spheroid morphology and behavior. For example, the presence of fibrous matrices is important in regulating hepatoma spheroid formation

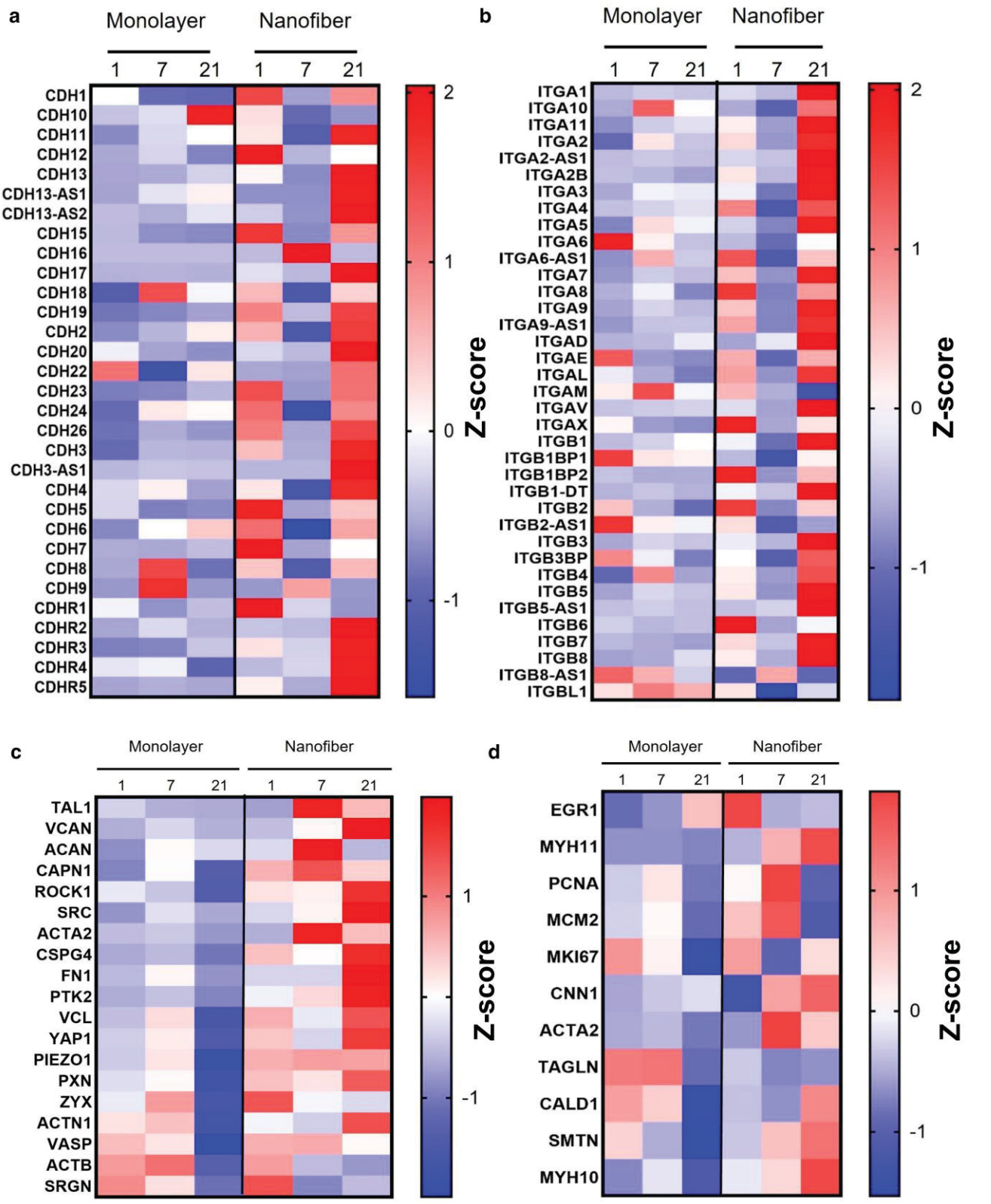

Fig. 5. Pericytes on nanofiber scaffolds up-regulate cadherin, integrin, mechanosensing, and contractility gene transcripts. Heatmaps of TPM Z-score bulk RNA-Seq data for a) cadherin genes, b) integrin genes, c) mechanosensing, and d) contractility genes shown at days 1, 7, and 21 postseeding on monolayer cultures and force nanofiber scaffolds. TPM, transcripts per million.

due to increased integrin–ECM binding (21, 66), spheroid disaggregation in ovarian cancer cell spheroids (67), and increased invasiveness of melanoma cell spheroids (22). Primary pericytes isolated from mouse lungs have been shown to respond to mechanical stimuli, and increasing the matrix stiffness induces differentiation into fibroblasts and the invasiveness of pericyte

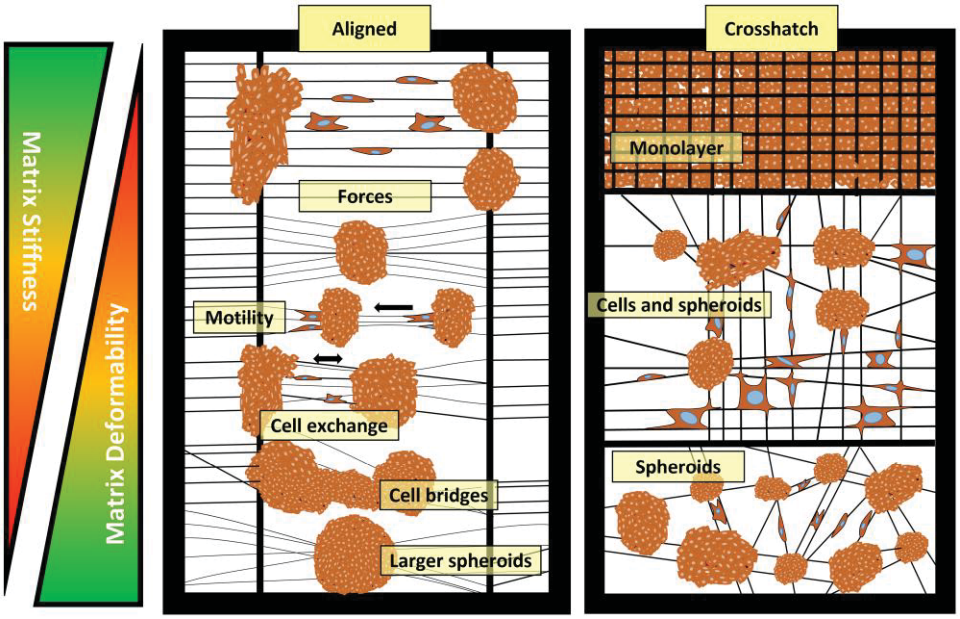

Fig. 6. Summary figure. Schematic illustrating spheroid formation, motility, and mergers with increasing fiber deformability (decreasing extracellular matrix stiffness) on aligned and crosshatch network of fibers. On aligned fibers, spheroids are pulled by cells and cellular exchange between spheroids leads to formation of cell bridges and larger spheroids. On crosshatch networks, high stiffness (low deformability) leads to formation of monolayers, while high fiber network deformability leads to spheroids with cellular exchange. Patterning of spheroids and monolayers adjacent to each other is achieved by tuning the deformability of fiber networks.

spheroids (19). In the present study, we evaluated spheroid formation by vasa vasorum-associated pericytes as a model system and found that matrix remodeling favored spheroid formation. Differently sized spheroids spontaneously assembled on the same scaffold, which contrasts with other methods of spheroid formation (e.g. hanging drop, agarose–poly-HEMA-coated substrates) with predetermined size and geometry.

Various processes such as morphogenesis, wound healing, and tumor formation involve a mode of cell migration known as collective cell migration (68–72). Previously, we have shown that "leader" and "follower" cells in single, chain, and collective modes migrate from a monolayer interfaced with an aligned and crosshatched network of fibers (72). Here, on aligned fiber networks, we found a remarkable ability of a single or a few cells to drag (pull) spheroids during migration. This form of migration by a cell is similar to collective cell migration initiated by leader/tip cells (73–76). Surprisingly, we also observed spheroids migrating without a leader cell, possibly due to challenges in identifying a leader cell from top-view imaging (a limitation of our study) or an unclear ability of spheroids to move as a whole. Notwithstanding, the observed migration of spheroids on and/or around fibers remains puzzling. Confocal images revealed that spheroid formation occurred by aggregation around the fibers (i.e. fibers were noted within spheroids), and our observation that cells pulled the spheroids suggests a sliding mode that would be possible only on a parallel arrangement of fibers. Indeed, spheroids were found to be predominantly nonmigratory at orthogonal *base* fibers in aligned fiber networks and on crosshatched networks of fibers. However, the nonmigratory spheroids were connected by fibers over large distances and actively exchanged cells between them.

Spheroid mergers have been documented in literature (16, 77–80). Kim et al. (16) have shown that spheroids formed spontaneously within hydrogels can merge through cellular bridges when separated by a distance of 100 μm. At 200-μm spacing, spheroids form cellular bridges without merger. At even longer separation distances (400 μm), cellular bridges do not form. In our work, we have demonstrated that spheroids can merge at even longer distances (400 μm and above), with cellular bridges forming at even longer distances (~2000 μm). We observed two distinct modes of spheroid mergers, depending on their size. Smaller spheroids on the aligned fiber networks merged through migration. In contrast, larger spheroids merged via cell exchange by forming a cell bridge through the exertion of significant forces and fiber remodeling. The morphogenic Boolean outcomes of mergers showed an increase in area of the resultant spheroid but with a decrease in circularity. The cases of three-spheroid mergers proceeded with spheroids on the same large diameter fiber merging first followed by merging with the distant third spheroid. In all mergers, the trigger point leading to the formation of cellular bridges remains unknown, especially with considerations to contact inhibition of locomotion (28). Spheroid merging is perplexing—individual spheroids form by cells coalescing to form a larger structure, while spheroid mergers proceed with the same individual spheroids disassociating and then coalescing again to form an even larger structure. In these mergers, the contributions of the orientation of cells and their nuclei remain unknown.

The mechanical force exertions of spheroids are a focal point of active research (20, 81–83). We calculated the forces exerted by individual spheroids on fiber scaffolds. During the initial stages of spheroid formation, cellular monolayers exert a larger force on the scaffold. We found a continuous drop in force exertion as cells assembled into 3D spheroidal structures. Once formed, the stiffness and matrix alignment in the fibers have been previously shown to cause collective invasion from the spheroids, thus causing sprouting in endothelial and melanoma cell spheroids (18, 22, 84). Inspired by these studies, we quantified the dynamics of cell exchange with spheroids and found higher cell efflux than influx over 24 h. The spheroid area remaining constant with a large outward cell flow suggests that the cells within the spheroid may be undergoing mitosis at a rate similar to the number of lost cells. This is confirmed with measurements showing an increase in area concomitant with a decrease in the efflux. Our fiber networks allowed us to quantify the

drop in spheroid force exertion when cells left the spheroid, indicating the contributory role of individual cells to spheroid forces. Single cells leaving the spheroids match our previous finding of a *recoil* invasion (efflux) of single cells from a monolayer, whereby the cells underwent a conditioning phase of forward–backward motion along the fiber, before escaping the spheroid in a slingshot manner, while a group of cells emerges collectively without recoil, implying strong cell–cell forces (72). We also observed groups of cells collectively leaving the spheroids, which has been described for cancer spheroids (85) and may have important implications during tissue remodeling and angiogenesis akin to the formation of endothelial tip cells (86).

Actin–myosin contractility can alter spheroid behavior and compaction in various cell types, such as human mesenchymal stem cells and breast and ovarian cancer cell lines (67, 87, 88). Pericytes wrap around blood vessels in the microvasculature, and their contractility helps to maintain vascular homeostasis and regulate blood flow (62). We confirmed that inhibiting actin–myosin contractility with Rho kinase caused a reversible destabilizing effect on pericyte spheroids, and prolonged inhibition prevented the 3D assembly of pericytes into spheroids. This finding is reminiscent, though distinct from findings in endothelial cell spheroids where Rho kinase inhibition caused cell migration away from spheroids (89). Thus, our data suggest that contractility plays a significant role in their ability to form and assemble into 3D structures and can induce morphological changes upon inhibition, potentially impacting pericyte spheroid putative functions. Indeed, the importance of pericyte contractility is an area of high interest (4, 58, 62, 90–94). The RNA-Seq analysis revealed striking shifts in gene expression profiles over time for pericyte spheroids on fiber networks, including several contractility-related genes, further exemplifying the importance of cell contractility in spheroid dynamics. We found several mechanosensing (*ROCK1*, *SRC*, and *YAP1*) and contractility (*SMTN*, *MYH11*, and *ACTA2*) genes up-regulated in fiber networks compared with monolayer cultures. For example, *ACTA2*, which encodes smooth muscle α-actin, has been implicated in multiple mechanosensing activities such as integrin recruitment at cell–matrix adhesions and the cell's ability to contract and generate forces required for matrix remodeling (95). The up-regulation of cadherins, integrins, and mechanosensing genes further supports that cell–cell, cell–matrix, and response to matrix biophysical cues temporally participate in spheroid assembly and morphogenesis. Similarly, the up-regulation of ROCK1 during spheroid formation closely aligns with our Rho kinase activity inhibition and restoration as a key regulator of spheroid assembly on fiber networks. We also observed a puzzling behavior that pericyte spheroids "beat" rhythmically during the third week of culture. Relatedly, pericyte function has been associated with regulating blood flow in the microvasculature, including at the microcirculatory level (62, 91–93). Blood pressure levels dictate to some degree pericyte density on microvessels, so that areas of increased blood pressure control the flow of blood upwards in humans at the lower part of the body (the torso and the legs) (94, 96). Thus, we speculate that dense pericyte structures as in spheroids may develop rhythmic contractions as part of their ability to meet blood pressure requirements.

Overall, we demonstrate that ECM-mimicking suspended fiber networks of varying diameters and architectures can be tuned to various configurations to interrogate the underlying mechanical principles governing the formation and maintenance of 3D spheroids. We show that matrix deformability and cell contractility captured by measurements of forces exerted by pericytes are two critical cues that work in tandem during the spontaneous assembly of cells into 3D structures in fibrous ECM environments. Spheroids can form among multiple cell types, and putative tissue specificity in function and behavior of spheroids that may exist among pericytes from different vascularized tissue beds could be revealed through further study. We envision that our findings linking matrix biology with spheroid dynamics may inspire studies and technologies aimed at spheroid-based translational applications.

Supplementary Material

Supplementary material is available at *PNAS Nexus* online.

Funding

A.S.N. acknowledges partial funding support from the National Science Foundation (grant nos. 2107332, 2119949, and 2422340) and the Institute of Critical Technologies and Science and Macromolecules Innovative Institute at Virginia Tech for supporting this study. Partial support for this work was provided by the NHLBI under award #HL131632 (J.A.P.), University of Pittsburgh Physicians, and the Department of Cardiothoracic Surgery, University of Pittsburgh (J.A.P.). A.S.N. and J.A.P. acknowledge support from NHLBI award #HL162822. Library generation and sequencing were performed in the Health Sciences Sequencing Core at UPMC Children's Hospital of Pittsburgh, Rangos Research Center. Services and instruments used in this project were graciously supported, in part, by the University of Pittsburgh, the Office of the Senior Vice Chancellor for Health Sciences, the Department of Pediatrics, the Institute for Precision Medicine, and the Richard K Mellon Foundation for Pediatric Research (RRID: SCR_023116).

Author Contributions

Sharan Sharma (Formal Analysis, Investigation, Methodology, Writing—original draft, Writing—review & editing), Atharva Agashe (Formal Analysis, Investigation, Methodology, Writing—review & editing), Jennifer C. Hill (Formal Analysis, Investigation, Methodology, Writing—review & editing), Keya Ganguly (Formal Analysis, Investigation), Puja Sharma (Formal Analysis, Investigation, Methodology), Tara D. Richards (Methodology), Weijian Huang (Formal Analysis), David J. Kaczorowski (Resources), Pablo G. Sanchez (Resources), Rakesh Kapania (Methodology), Julie A. Phillippi (Conceptualization, Data curation, Formal Analysis, Funding acquisition, Investigation, Methodology, Project administration, Resources, Software, Supervision, Validation, Visualization, Writing—original draft, Writing—review & editing), and Amrinder S. Nain (Conceptualization, Data curation, Formal Analysis, Funding acquisition, Investigation, Methodology, Project administration, Resources, Software, Supervision, Validation, Visualization, Writing—original draft, Writing—review & editing).

Preprints

This manuscript was posted on a preprint: https://www.biorxiv.org/content/10.1101/2022.08.02.502506v1.

Data Availability

All data are included in the manuscript and/or supporting information. RNA-Seq raw data files are deposited in the GEO repository accession number GSE284140.

References

1 Duval K, *et al.* 2017. Modeling physiological events in 2D vs. 3D cell culture. *Physiology*. 32:266–277.
2 Baker BM, Chen CS. 2012. Deconstructing the third dimension-how 3D culture microenvironments alter cellular cues. *J Cell Sci*. 125:3015–3024.
3 Shao C, *et al.* 2020. Development of cell spheroids by advanced technologies. *Adv Mater Technol*. 5:2000183.
4 Achilli TM, Meyer J, Morgan JR. 2012. Advances in the formation, use and understanding of multi-cellular spheroids. *Expert Opin Biol Ther*. 12:1347–1360.
5 Mueller-Klieser W. 1987. Multicellular spheroids—a review on cellular aggregates in cancer research. *J Cancer Res Clin Oncol*. 113:101–122.
6 Zanoni M, *et al.* 2020. Modeling neoplastic disease with spheroids and organoids. *J Hematol Oncol*. 13:97.
7 Sakalem ME, De Sibio MT, da Costa FADS, de Oliveira M. 2021. Historical evolution of spheroids and organoids, and possibilities of use in life sciences and medicine. *Biotechnol J*. 16:e2000463.
8 Ong CS, *et al.* 2018. In vivo therapeutic applications of cell spheroids. *Biotechnol Adv*. 36:494–505.
9 Fennema E, Rivron N, Rouwkema J, van Blitterswijk C, De Boer J. 2013. Spheroid culture as a tool for creating 3D complex tissues. *Trends Biotechnol*. 31:108–115.
10 Kelm JM, Timmins NE, Brown CJ, Fussenegger M, Nielsen LK. 2003. Method for generation of homogeneous multicellular tumor spheroids applicable to a wide variety of cell types. *Biotechnol Bioeng*. 83:173–180.
11 Jeong Kim S, Kim EM, Yamamoto M, Park H, Shin H. 2020. Engineering multi-cellular spheroids for tissue engineering and regenerative medicine. *Adv Healthc Mater*. 9:2000608.
12 Ruedinger F, Lavrentieva A, Blume C, Pepelanova I, Scheper T. 2015. Hydrogels for 3D mammalian cell culture: a starting guide for laboratory practice. *Appl Microbiol Biotechnol*. 99:623–636.
13 Li R, *et al.* 2022. Fibrinogen improves liver function via promoting cell aggregation and fibronectin assembly in hepatic spheroids. *Biomaterials*. 280:121266.
14 Shin JY, *et al.* 2012. Efficient formation of cell spheroids using polymer nanofibers. *Biotechnol Lett*. 34:795–803.
15 Wei J, Lu J, Liu Y, Yan S, Li X. 2016. Spheroid culture of primary hepatocytes with short fibers as a predictable in vitro model for drug screening. *J Mater Chem B*. 4:7155–7167.
16 Ahmad T, *et al.* 2017. Hybrid-spheroids incorporating ECM like engineered fragmented fibers potentiate stem cell function by improved cell/cell and cell/ECM interactions. *Acta Biomater*. 64: 161–175.
17 Youssef J, Nurse AK, Freund LB, Morgan JR. 2011. Quantification of the forces driving self-assembly of three-dimensional microtissues. *Proc Natl Acad Sci U S A*. 108:6993–6998.
18 Korff T, Augustin HG. 1999. Tensional forces in fibrillar extracellular matrices control directional capillary sprouting. *J Cell Sci*. 112:3249–3258.
19 Feng F, Feng X, Zhang D, Li Q, Yao L. 2021. Matrix stiffness induces pericyte-fibroblast transition through YAP activation. *Front Pharmacol*. 12:1370.
20 Boot RC, Koenderink GH, Boukany PE. 2021. Spheroid mechanics and implications for cell invasion. *Adv Phys X*. 6:1978316.
21 Efremov YM, *et al.* 2021. Mechanical properties of cell sheets and spheroids: the link between single cells and complex tissues. *Biophys Rev*. 13:541–561.
22 Ahmadzadeh H, *et al.* 2017. Modeling the two-way feedback between contractility and matrix realignment reveals a nonlinear mode of cancer cell invasion. *Proc Natl Acad Sci U S A*. 114: E1617–E1626.
23 Kopanska KS, Alcheikh Y, Staneva R, Vignjevic D, Betz T. 2016. Tensile forces originating from cancer spheroids facilitate tumor invasion. *PLoS One*. 11:e0156442.
24 Rauff A, LaBelle SA, Strobel HA, Hoying JB, Weiss JA. 2019. Imaging the dynamic interaction between sprouting microvessels and the extracellular matrix. *Front Physiol*. 10:455548.
25 Tevis KM, Colson YL, Grinstaff MW. 2017. Embedded spheroids as models of the cancer microenvironment. *Adv Biosyst*. 1: 1700083.
26 Dey M, Ayan B, Yurieva M, Unutmaz D, Ozbolat IT. 2021. Studying tumor angiogenesis and cancer invasion in a three-dimensional vascularized breast cancer micro-environment. *Adv Biol*. 5:2100090.
27 Han W, *et al.* 2016. Oriented collagen fibers direct tumor cell intravasation. *Proc Natl Acad Sci U S A*. 113:11208–11213.
28 Singh J, Pagulayan A, Camley BA, Nain AS. 2021. Rules of contact inhibition of locomotion for cells on suspended nanofibers. *Proc Natl Acad Sci U S A*. 118:e2011815118.
29 Jana A, *et al.* 2023. Mitotic outcomes and errors in fibrous environments. *Proc Natl Acad Sci U S A*. 120:e2120536120.
30 Jana A, *et al.* 2022. Sculpting rupture-free nuclear shapes in fibrous environments. *Adv Sci*. 9:2203011.
31 Mukherjee A, *et al.* 2023. Actin filaments couple the protrusive tips to the nucleus through the I-BAR domain protein IRSp53 during the migration of cells on 1D fibers. *Adv Sci*. 10:2207368.
32 Graybill PM, Jana A, Kapania RK, Nain AS, Davalos RV. 2021. Single cell forces after electroporation. *ACS Nano*. 15:2554–2568.
33 Fantini DA, *et al.* 2024. Overcoming big bottlenecks in vascular regeneration. *Commun Biol*. 7:876.
34 Nain AS, *et al.* 2008. Control of cell behavior by aligned micro/nanofibrous biomaterial scaffolds fabricated by spinneret-based tunable engineered parameters (STEP) technique. *Small*. 4: 1153–1159.
35 Billaud M, Hill JC, Richards TD, Gleason TG, Phillippi JA. 2018. Medial hypoxia and adventitial vasa vasorum remodeling in human ascending aortic aneurysm. *Front Cardiovasc Med*. 5:124.
36 Nain AS, Sitti M, Jacobson A, Kowalewski T, Amon C. 2009. Dry spinning based spinneret based tunable engineered parameters (STEP) technique for controlled and aligned deposition of polymeric nanofibers. *Macromol Rapid Commun*. 30:1406–1412.
37 Wang J, Nain AS. 2014. Suspended micro/nanofiber hierarchical biological scaffolds fabricated using non-electrospinning STEP technique. *Langmuir*. 30:13641–13649.
38 Wang J, Hou J, Marquez E, Moore RB, Nain AS. 2014. Aligned assembly of nano and microscale polystyrene tubes with controlled morphology. *Polymer*. 55:3008–3014.
39 Ushiki T. 2002. Collagen fibers, reticular fibers and elastic fibers. A comprehensive understanding from a morphological viewpoint. *Arch Histol Cytol*. 65:109–126.
40 Fernández M, *et al.* 2002. Small-angle x-ray scattering studies of human breast tissue samples. *Phys Med Biol*. 47:577–592.
41 Doyle AD, Wang FW, Matsumoto K, Yamada KM. 2009. One-dimensional topography underlies three-dimensional fibrillar cell migration. *J Cell Biol*. 184:481–490.
42 Conklin MW, *et al.* 2011. Aligned collagen is a prognostic signature for survival in human breast carcinoma. *Am J Pathol*. 178: 1221–1232.
43 Keely P, Nain A. 2015. Capturing relevant extracellular matrices for investigating cell migration. *F1000Res*. 4:1408.

44 Weigelin B, Bakker G-J, Friedl P. 2014. Intravital third harmonic generation microscopy of collective melanoma cell invasion. *IntraVital*. 1:32–43.
45 Glentis A, *et al.* 2017. Cancer-associated fibroblasts induce metalloprotease-independent cancer cell invasion of the basement membrane. *Nat Commun*. 8:924.
46 Clark AG, Vignjevic DM. 2015. Modes of cancer cell invasion and the role of the microenvironment. *Curr Opin Cell Biol*. 36:13–22.
47 Taylor EN, Hoffman MP, Aninwene GE, Gilbert RJ. 2015. Patterns of intersecting fiber arrays revealed in whole muscle with generalized Q-space imaging. *Biophys J*. 108:2740–2749.
48 Yamada KM, *et al.* 2019. Extracellular matrix dynamics in cell migration, invasion and tissue morphogenesis. *Int J Exp Pathol*. 100: 144–152.
49 Friedl P, Wolf K. 2010. Plasticity of cell migration: a multiscale tuning model. *J Cell Biol*. 188:11–19.
50 Harley BAC, *et al.* 2008. Microarchitecture of three-dimensional scaffolds influences cell migration behavior via junction interactions. *Biophys J*. 95:4013–4024.
51 Durgam S, Singh B, Cole SL, Brokken MT, Stewart M. 2020. Quantitative assessment of tendon hierarchical structure by combined second harmonic generation and immunofluorescence microscopy. *Tissue Eng Part C Methods*. 26:253–262.
52 Sheets K, Wang J, Zhao W, Kapania R, Nain AS. 2016. Nanonet force microscopy for measuring cell forces. *Biophys J*. 111: 197–207.
53 Koons B, *et al.* 2017. Cancer protrusions on a tightrope: nanofiber curvature contrast quantitates single protrusion dynamics. *ACS Nano*. 11:12037–12048.
54 Padhi A, *et al.* 2020. Force-exerting perpendicular lateral protrusions in fibroblastic cell contraction. *Commun Biol*. 3:390.
55 Jana A, *et al.* 2019. Crosshatch nanofiber networks of tunable interfiber spacing induce plasticity in cell migration and cytoskeletal response. *FASEB J*. 33:10618–10632.
56 Padhi A, *et al.* 2021. Cell fragment formation, migration, and force exertion on extracellular mimicking fiber nanonets. *Adv Biol*. 5: 2000592. https://doi.org/10.1002/adbi.202000592
57 Billaud M, *et al.* 2017. Classification and functional characterization of vasa vasorum-associated perivascular progenitor cells in human aorta. *Stem Cell Rep*. 9:292–303.
58 Wintruba KL, *et al.* 2022. Adventitia-derived extracellular matrix hydrogel enhances contractility of human vasa vasorum-derived pericytes via α2β1 integrin and TGFβ receptor. *J Biomed Mater Res Part A*. 110:1912–1920.
59 Hall A, *et al.* 2017. Nanonet force microscopy for measuring forces in single smooth muscle cells of the human aorta. *Mol Biol Cell*. 28:1894–1900.
60 Gerhardt H, Betsholtz C. 2003. Endothelial-pericyte interactions in angiogenesis. *Cell Tissue Res*. 314:15–23.
61 Armulik A, Abramsson A, Betsholtz C. 2005. Endothelial/pericyte interactions. *Circ Res*. 97:512–523.
62 Dessalles CA, Babataheri A, Barakat AI. 2021. Pericyte mechanics and mechanobiology. *J Cell Sci*. 134:jcs240226.
63 Bodnar RJ, Satish L. 2018. Targeting pericytes to improve wound healing outcomes. *Curr Pathobiol Rep*. 6:117–123.
64 Van Dijk CGM, *et al.* 2015. The complex mural cell: pericyte function in health and disease. *Int J Cardiol*. 190:75–89.
65 Kang E, Shin JW. 2016. Pericyte-targeting drug delivery and tissue engineering. *Int J Nanomedicine*. 11:2397–2406.
66 Lin RZ, Chou LF, Chien CCM, Chang HY. 2006. Dynamic analysis of hepatoma spheroid formation: roles of E-cadherin and β1-integrin. *Cell Tissue Res*. 324:411–422.
67 McKenzie AJ, *et al.* 2018. The mechanical microenvironment regulates ovarian cancer cell morphology, migration, and spheroid disaggregation. *Sci Rep*. 8:7228.
68 Christiansen JJ, Rajasekaran AK. 2006. Reassessing epithelial to mesenchymal transition as a prerequisite for carcinoma invasion and metastasis. *Cancer Res*. 66:8319–8326.
69 Friedl P, Gilmour D. 2009. Collective cell migration in morphogenesis, regeneration and cancer. *Nat Rev Mol Cell Biol*. 10: 445–457.
70 Scarpa E, Mayor R. 2016. Collective cell migration in development. *J Cell Biol*. 212:143–155.
71 Poujade M, *et al.* 2007. Collective migration of an epithelial monolayer in response to a model wound. *Proc Natl Acad Sci U S A*. 104: 15988–15993.
72 Sharma P, *et al.* 2017. Aligned fibers direct collective cell migration to engineer closing and nonclosing wound gaps. *Mol Biol Cell*. 28:2579–2588.
73 Haeger A, Wolf K, Zegers MM, Friedl P. 2015. Collective cell migration: guidance principles and hierarchies. *Trends Cell Biol*. 25: 556–566.
74 Carey SP, Starchenko A, McGregor AL, Reinhart-King CA. 2013. Leading malignant cells initiate collective epithelial cell invasion in a three-dimensional heterotypic tumor spheroid model. *Clin Exp Metastasis*. 30:615–630.
75 Khalil AA, Friedl P. 2010. Determinants of leader cells in collective cell migration. *Integr Biol (Camb)*. 2:568–574. https://doi.org/10.1039/c0ib00052c
76 Mayor R, Etienne-Manneville S. 2016. The front and rear of collective cell migration. *Nat Rev Mol Cell Biol*. 17:97–109.
77 Cui H, *et al.* 2021. Assembly of multi-spheroid cellular architectures by programmable droplet merging. *Adv Mater*. 33:2006434.
78 Kosheleva NV, *et al.* 2020. Cell spheroid fusion: beyond liquid drops model. *Sci Rep*. 10:12614.
79 Tomasi RFX, Sart S, Champetier T, Baroud CN. 2020. Individual control and quantification of 3D spheroids in a high-density microfluidic droplet array. *Cell Rep*. 31:107670.
80 Pan R, *et al.* 2023. Recapitulating the drifting and fusion of two-generation spheroids on concave agarose microwells. *Int J Mol Sci*. 24:11967.
81 Lee W, *et al.* 2019. Dispersible hydrogel force sensors reveal patterns of solid mechanical stress in multicellular spheroid cultures. *Nat Commun*. 10:144.
82 Mark C, *et al.* 2020. Collective forces of tumor spheroids in three-dimensional biopolymer networks. *Elife*. 9:e51912.
83 Blumlein A, Williams N, McManus JJ. 2017. The mechanical properties of individual cell spheroids. *Sci Rep*. 7:7346.
84 Crosby CO, Zoldan J. 2019. Mimicking the physical cues of the ECM in angiogenic biomaterials. *Regen Biomater*. 6:61–73.
85 Audoin M, Søgaard MT, Jauffred L. 2022. Tumor spheroids accelerate persistently invading cancer cells. *Sci Rep*. 12:14713.
86 Heiss M, *et al.* 2015. Endothelial cell spheroids as a versatile tool to study angiogenesis in vitro. *FASEB J*. 29:3076–3084.
87 Tsai AC, Liu Y, Yuan X, Ma T. 2015. Compaction, fusion, and functional activation of three-dimensional human mesenchymal stem cell aggregate. *Tissue Eng Part A*. 21:1705–1719.
88 Devanny AJ, Vancura MB, Kaufman LJ. 2021. Exploiting differential effects of actomyosin contractility to control cell sorting among breast cancer cells. *Mol Biol Cell*. 32:ar24.
89 Breyer J, *et al.* 2012. Inhibition of Rho kinases increases directional motility of microvascular endothelial cells. *Biochem Pharmacol*. 83:616–626.
90 Rucker HK, Wynder HJ, Thomas WE. 2000. Cellular mechanisms of CNS pericytes. *Brain Res Bull*. 51:363–369.

91 Methner C, *et al*. 2019. Pericyte constriction underlies capillary derecruitment during hyperemia in the setting of arterial stenosis. *Am J Physiol Hear Circ Physiol*. 317:H255–H263.
92 Dalkara T, Gursoy-Ozdemir Y, Yemisci M. 2011. Brain microvascular pericytes in health and disease. *Acta Neuropathol*. 122:1–9.
93 Gökçinar-Yagci B, Uçkan-Çetinkaya D, Çelebi-Saltik B. 2015. Pericytes: properties, functions and applications in tissue engineering. *Stem Cell Rev Rep*. 11:549–559.
94 Bergers G, Song S. 2005. The role of pericytes in blood-vessel formation and maintenance. *Neuro Oncol*. 7:452–464.
95 Massett MP, *et al*. 2020. Loss of smooth muscle α-actin effects on mechanosensing and cell–matrix adhesions. *Exp Biol Med*. 245: 374–384.
96 Sims D, Horne MM, Creighan M, Donald A. 1994. Heterogeneity of pericyte populations in equine skeletal muscle and dermal microvessels: a quantitative study. *Anat Histol Embryol*. 23:232–238.